# Singular-Perturbation Control of a Tendon-Driven Soft Robot
## Theory and Experiments

Ribeiro, Lucas Novaki; Borja, Pablo; Santina, Cosimo Della; Deutschmann, Bastian

**DOI**
10.1109/TCST.2025.3546564

**Publication date**
2025

**Document Version**
Final published version

**Published in**
IEEE Transactions on Control Systems Technology

**Citation (APA)**
Ribeiro, L. N., Borja, P., Santina, C. D., & Deutschmann, B. (2025). Singular-Perturbation Control of a Tendon-Driven Soft Robot: Theory and Experiments. *IEEE Transactions on Control Systems Technology*, *33*(5), 1929-1936. https://doi.org/10.1109/TCST.2025.3546564

# Singular-Perturbation Control of a Tendon-Driven Soft Robot: Theory and Experiments

Lucas Novaki Ribeiro, Pablo Borja, *Senior Member, IEEE*, Cosimo Della Santina, *Senior Member, IEEE*, and Bastian Deutschmann

***Abstract*— The existing model-based control strategies for tendon-driven continuum soft robots neglect the dynamics of the actuation system. Nevertheless, such dynamics have an important impact on the closed-loop performance. This work analyzes the influence of the actuation dynamics in tendon-driven continuum soft robots performing trajectory-tracking tasks. To this end, we use singular perturbation (SP) theory to design controllers that account for such dynamics. We provide the analytical formulation of the SP controllers and their in-depth experimental validation. Additionally, we use high- and low-stiffness tendons to experimentally compare the performance of the proposed SP controllers against traditional feedback control schemes that disregard the actuation dynamics. The experimental results show that SP controllers outperform the approaches that neglect the actuation dynamics by reducing oscillations and achieving lower errors without relying on high gains. Furthermore, it is shown that neglecting the actuation dynamics may lead to instability when the tendons have a low stiffness coefficient.**

***Index Terms*— Continuum soft robots, model-based control, singular perturbation, tendon-driven robots.**

## I. Introduction

THE compliant nature of soft robots is ideal for guaranteeing a safe human-robot interaction, robust locomotion, and adaptability to unstructured environments. These properties can only be fully exploited through appropriate control designs, where model-based approaches are appealing because they can consider the physical properties of soft robots while ensuring a less destructive implementation process than the one resulting from learning strategies. Nonetheless, there are several challenges in modeling and model-based control of soft robots, for example, developing models that accurately capture the behavior of these robots with infinite degrees of freedom, the inherently underactuated nature of these systems, and their highly nonlinear behavior due to their compliant structures [1]. These challenges have favored the faster development of learning approaches for controlling soft robots. Nonetheless, developing model-based strategies is still paramount for advancing soft robotics. While several recent references, such as [2] and [3], propose relatively general model-based strategies for controlling soft robots, the actuation subsystem dynamics are often neglected. Notably, such dynamics significantly affect the closed-loop system's performance, as shown in [4] for a pneumatic-actuated system.

This brief focuses on tendon-driven soft robots. As their name indicates, these soft robots are actuated by tendons or cables. Two comprehensive surveys studying these systems are [1] and [5]. Similarly, Rao et al. [6] and Janabi-Sharifi et al. [7] provided an overview of modeling strategies for tendon-driven continuum soft robots. The references mentioned, mainly [1], discuss the Euler–Lagrange representation of soft robots. Concerning model-based control strategies for these systems, several approaches have been proposed and experimentally validated (see, for instance, [8], [9], [10], [11]). Nonetheless, none of these approaches consider the effect of the actuation dynamics on the closed-loop system. Such dynamics comprise the motors' behavior and their interconnection with the robot's body through the tendons. We stress that the actuation dynamics greatly influence the closed-loop performance, especially when low-stiffness tendons are utilized. Hence, model-based control strategies accounting for the actuation dynamics in tendon-driven soft robots are a critical missing piece in applications involving these systems.

This brief proposes model-based controllers that account for the actuation dynamics in planar tendon-driven continuum soft robots. To this end, we represent the behavior of the continuum segment via a constant curvature (CC) approximation (see [12]). Then, by considering that the actuation subsystem evolves much faster than the continuum segment, we propose a singular perturbation (SP) approach (see, for instance, [13], [14]) to design controllers that consider the elastic couplings between the robot's body and the actuators. The use of SP approaches to improve performance in robotics has been explored in [15] and [16]. Similarly, several references (e.g., [17], [18]) have studied the effect of elastic tendons on the performance of rigid robots; however, a model-based control approach that accounts for the rich actuation dynamics in tendon-driven systems is new for soft robots. Similarly, no SP control designs for soft robots seem to have been reported. The main contributions of this work are listed below.

Received 27 August 2024; revised 21 January 2025; accepted 22 February 2025. Date of publication 11 March 2025; date of current version 20 August 2025. This work was supported by German Research Foundation (DFG), as part of the Priority Program 2100 Soft Material Robotic Systems under Grant 405032572. The work of Cosimo Della Santina was supported by the Horizon Europe Program from Project EMERGE under Grant 101070918. Recommended by Associate Editor Y. Pan. *(Corresponding author: Pablo Borja.)*

Lucas Novaki Ribeiro and Bastian Deutschmann are with the Institute of Robotics and Mechatronics, German Aerospace Center (DLR), 82234 Weßling, Germany (e-mail: lnovaki.ribeiro@gmail.com; bastian.Deutschmann@dlr.de).

Pablo Borja is with the School of Engineering, Computing and Mathematics, University of Plymouth, PL4 8AA Plymouth, U.K. (e-mail: pablo.borjarosales@plymouth.ac.uk).

Cosimo Della Santina is with the Department of Cognitive Robotics, Delft University of Technology, 2628 CD Delft, The Netherlands, and also with the Institute of Robotics and Mechatronics, German Aerospace Center (DLR), 82234 Weßling, Germany (e-mail: c.dellasantina@tudelft.nl).

This article has supplementary downloadable material available at https://doi.org/10.1109/TCST.2025.3546564, provided by the authors.

Digital Object Identifier 10.1109/TCST.2025.3546564

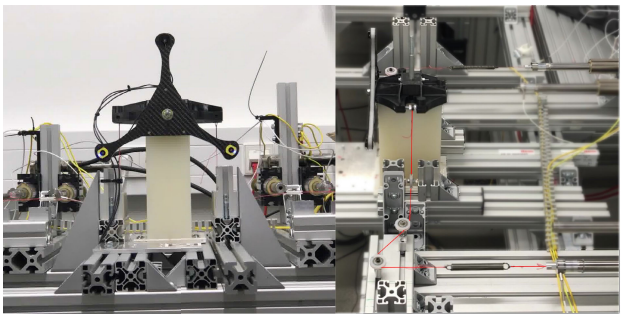

Fig. 1. In this work, we look into model-based control strategies for the tendon-actuated soft segment depicted in the pictures. This system is representative of the challenge we encounter on generic tendon-actuated soft robots while being manageable enough to serve as the base of an in-depth study. Note the extension spring attaching the tendon in the side view of the setup (right).

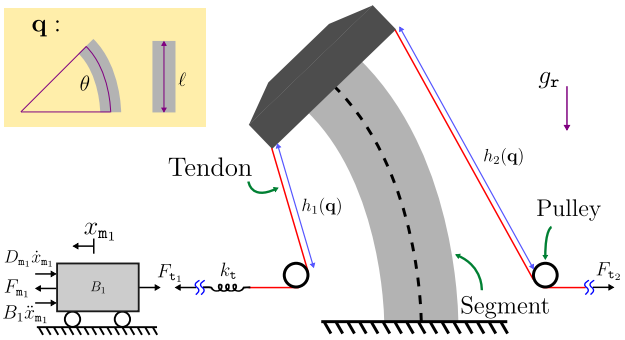


Fig. 2. Schematic of the soft robot. The graphical description of the coordinates $\boldsymbol{q}$ is given in the upper left corner. The dynamics of the linear motor actuator are represented as a mass-spring-damper system.

1) The design of (model-based) SP controllers to deal with the actuation dynamics in planar tendon-driven soft robots. Such controllers perform better than those that neglect the actuation dynamics, contributing to the practical operation of soft robots.
2) The experimental validation of the proposed controllers using the setup depicted in Fig. 1. Additionally, we provide an in-depth analysis of the effect of actuation dynamics and couplings between the robot and the actuators on closed-loop performance.
3) A detailed comparison of the experimental results obtained with the proposed controllers and common control schemes that neglect the actuation dynamics.

The rest of the brief is organized as follows. Section II provides the model of the system and the problem formulation. Then, Section III proposes the control strategy that solves the trajectory tracking problem while considering the couplings between the robot and the actuators. Section IV is devoted to the experimental validation of the proposed controllers. Moreover, in this section, we compare the closed-loop performance of our approach with existing control designs. Finally, some concluding remarks are given in Section V.

*Notation:* Bold font in mathematical expressions is used to denote matrices and vectors. In particular, the symbol $\mathbf{0}$ represents a vector or matrix of appropriate dimensions, the elements of which are zeros. Subscripts in typewriter font are part of the name of the function, vector, or matrix. The subscript $i$ is reserved to denote the $i$th element of a vector. We adopt Newton's notation for differentiation with respect to time. Hence, $\dot{f} = (df(t))/(dt)$.

*Caveat:* When clear from the context, we omit the arguments of the functions to ease the readability.

## II. Modeling and Problem Statement

Consider a tendon-driven soft robot consisting of a compliant segment, which is elastically coupled—via the tendons—to the actuators. The schematic of the system is shown in Fig. 2. We model the robot via a CC approximation, that is, the base and tip of the compliant segment are connected by the arc $\theta \in \mathbb{R}$. We stress that this kind of approximation stands out for its simplicity while being capable of describing the behavior of compliant structures reasonably accurately [12]. Additionally, we consider a linear elastic deformation along the central axis of the segment, denoted by $\ell \in \mathbb{R}$. Hence, the configuration of the soft segment is described by the variables (see Fig. 2)

$$\boldsymbol{q} = \begin{bmatrix} \theta & \ell \end{bmatrix}^\top \in \mathbb{R}^2. \tag{1}$$

Furthermore, the behavior of the robot is characterized via the Euler–Lagrange formalism, resulting in the dynamics

$$\begin{aligned} \boldsymbol{M}(\boldsymbol{q})\ddot{\boldsymbol{q}} + \boldsymbol{C}(\boldsymbol{q},\dot{\boldsymbol{q}})\dot{\boldsymbol{q}} + \boldsymbol{D}\dot{\boldsymbol{q}} + \boldsymbol{K}\boldsymbol{q} + \boldsymbol{g}(\boldsymbol{q}) \\ = -\boldsymbol{P}^\top(\boldsymbol{q})\boldsymbol{F}_{\mathrm{t}}(\boldsymbol{x}_{\mathrm{m}},\boldsymbol{q}) \end{aligned} \tag{2}$$

where $\boldsymbol{x}_{\mathrm{m}} \in \mathbb{R}^2$ is the vector of motors' positions (displacements); $\boldsymbol{M}{:}\mathbb{R}^2 \to \mathbb{R}^{2\times 2}$ is the mass inertia matrix, which is positive definite; the matrix $\boldsymbol{C}{:}\mathbb{R}^2 \times \mathbb{R}^2 \to \mathbb{R}^{2\times 2}$ is related to the centrifugal and Coriolis terms; the segment's damping matrix $\boldsymbol{D} \in \mathbb{R}^{2\times 2}$ is constant, diagonal, and positive definite; $\boldsymbol{K} \in \mathbb{R}^{2\times 2}$ denotes the stiffness matrix related to the segment, which is also constant, diagonal, and positive definite; $\boldsymbol{g}{:}\mathbb{R}^2 \to \mathbb{R}^2$ is the vector of forces due to gravity; $\boldsymbol{P}{:}\mathbb{R}^2 \to \mathbb{R}^{2\times 2}$ is the Jacobian matrix associated with the tendons, which is invertible; $\boldsymbol{F}_{\mathrm{t}}{:}\mathbb{R}^2 \times \mathbb{R}^2 \to \mathbb{R}^2$ is the vector of tension forces due to the tendons. We recall that the matrix $\dot{\boldsymbol{M}} - 2\boldsymbol{C}(\boldsymbol{q},\dot{\boldsymbol{q}})$ is skew-symmetric (see [19]).

To derive $\boldsymbol{P}(\boldsymbol{q})$, we assume that the radii of the pulleys are negligible. Hence, we consider a point-wise redirection of the tendons. Moreover, we consider linear elastic tendons, while the associated tension forces are given by the following equation:

$$\boldsymbol{F}_{\mathrm{t}}(\boldsymbol{x}_{\mathrm{m}},\boldsymbol{q}) = \boldsymbol{K}_{\mathrm{t}}\left[\boldsymbol{x}_{\mathrm{m}} - \boldsymbol{L}_0 + \boldsymbol{h}(\boldsymbol{q})\right] \tag{3}$$

where $\boldsymbol{L}_0 \in \mathbb{R}^2$ represents the length of the tendons at rest; $\boldsymbol{K}_{\mathrm{t}} = \boldsymbol{I}_2 k_{\mathrm{t}}$ denotes the stiffness matrix associated with the tendons, where $k_{\mathrm{t}} \in \mathbb{R}_+$ is the stiffness coefficient of each tendon, which is assumed to be the same for every tendon; $\boldsymbol{h}{:}\mathbb{R}^2 \to \mathbb{R}^2$ captures the displacement of the tendon due to the configuration of the segment. Hence

$$\boldsymbol{P}(\boldsymbol{q}) = \frac{\partial \boldsymbol{h}(\boldsymbol{q})}{\partial \boldsymbol{q}}. \tag{4}$$

We neglect the pulleys' mass and any related dissipation phenomena. Hence, the dynamics of the linear motor actuators are given by the following equation:

$$\boldsymbol{B}\ddot{\boldsymbol{x}}_{\mathrm{m}} + \boldsymbol{D}_{\mathrm{m}}\dot{\boldsymbol{x}}_{\mathrm{m}} + \boldsymbol{F}_{\mathrm{t}}(\boldsymbol{x}_{\mathrm{m}},\boldsymbol{q}) = \boldsymbol{F}_{\mathrm{m}} \tag{5}$$

where $\boldsymbol{B} \in \mathbb{R}^{2\times 2}$ is a diagonal—and positive definite—matrix whose nonzero elements are the inertias of the motors; $\boldsymbol{D}_{\mathrm{m}} \in \mathbb{R}^{2\times 2}$ is the damping matrix associated with the motors, which is positive definite and diagonal; $\boldsymbol{F}_{\mathrm{m}} \in \mathbb{R}^2$ represents the control input vector.

*Problem Formulation:* Given the system described by (2), (3), and (5), design a controller $\boldsymbol{F}_{\mathrm{m}}(\boldsymbol{q}, \dot{\boldsymbol{q}}, \boldsymbol{x}_{\mathrm{m}}, \dot{\boldsymbol{x}}_{\mathrm{m}})$ such that the closed-loop system tracks the desired (feasible) trajectory. Regarding the trajectory to be tracked, we consider the following two cases.

1) The trajectory is discretized by a finite amount of points (configurations) denoted by $\boldsymbol{q}_\star \in \mathbb{R}^2$. Hence, the robot must reach these points sequentially, exhibiting a point-to-point motion that describes the desired trajectory.
2) The trajectory is a time-varying (smooth) curve denoted by $\boldsymbol{q}_{\mathrm{d}}{:}\mathbb{R}_{\geq 0} \to \mathbb{R}^2$. Thus, the trajectories of the robot must converge to the desired one, that is, $\lim_{t\to\infty} \boldsymbol{q}(t) = \boldsymbol{q}_{\mathrm{d}}$.

*Remark 1:* The problem and theoretical developments are formulated for a single-segment robot with two degrees of freedom because the controllers are experimentally validated in a system with these characteristics. However, the analysis and results can be scaled to robots consisting of multiple segments.

## III. Control Design

The dynamics associated with the actuators are considerably faster than the dynamics of the robot's body, yielding an underactuated system with two different time scales. Hence, we adopt an SP approach (see [13], [14], [20]) to analyze and control the resulting system. In particular, a boundary layer (BL) model—corresponding to the fast dynamics—and a quasisteady-state (QSS) model—corresponding to the slow dynamics—can be derived for the soft mechanism. The developments of this section are inspired by the SP results reported in [15] and [18]. We refer the reader to those papers for further details on SP results in robotics.

The fast and slow dynamics—corresponding to the motors and the compliant body of the robot, respectively—are coupled through $\boldsymbol{F}_{\mathrm{t}}(\boldsymbol{x}, \boldsymbol{q})$, given in (3). Hence, following the SP method adopted in [15], we rewrite the mentioned expression as follows:

$$\boldsymbol{F}_{\mathrm{t}}(\boldsymbol{x}_{\mathrm{m}}, \boldsymbol{q}) = \frac{\boldsymbol{K}_0}{\epsilon^2}\left[\boldsymbol{x}_{\mathrm{m}} - \boldsymbol{p}(\boldsymbol{q})\right] \tag{6}$$

where $\boldsymbol{K}_0 \in \mathbb{R}^{2\times 2}$ is a (diagonal) positive definite matrix, $\epsilon$ is a small positive constant, and

$$\boldsymbol{p}(\boldsymbol{q}) := \boldsymbol{L}_0 - \boldsymbol{h}(\boldsymbol{q}). \tag{7}$$

The objective is to express the system's behavior in terms of the BL and QSS models. To this end, we consider the new state variables $\boldsymbol{q}$, $\dot{\boldsymbol{q}}$, $\boldsymbol{F}_{\mathrm{t}}$, and $\dot{\boldsymbol{F}}_{\mathrm{t}}$—henceforth, the arguments $\boldsymbol{x}_{\mathrm{m}}$ and $\boldsymbol{q}$ are dropped from $\boldsymbol{F}_{\mathrm{t}}$. Then, manipulating (6), we obtain

$$\dot{\boldsymbol{x}}_{\mathrm{m}} = \epsilon^2 \boldsymbol{K}_0^{-1}\dot{\boldsymbol{F}}_{\mathrm{t}} + \dot{\boldsymbol{p}}; \quad \ddot{\boldsymbol{x}}_{\mathrm{m}} = \epsilon^2 \boldsymbol{K}_0^{-1}\ddot{\boldsymbol{F}}_{\mathrm{t}} + \ddot{\boldsymbol{p}}. \tag{8}$$

Substituting (8) into (5) yields

$$\boldsymbol{B}\left(\epsilon^2 \boldsymbol{K}_0^{-1}\ddot{\boldsymbol{F}}_{\mathrm{t}} + \ddot{\boldsymbol{p}}\right) + \boldsymbol{D}_{\mathrm{m}}\left(\epsilon^2 \boldsymbol{K}_0^{-1}\dot{\boldsymbol{F}}_{\mathrm{t}} + \dot{\boldsymbol{p}}\right) + \boldsymbol{F}_{\mathrm{t}} = \boldsymbol{F}_{\mathrm{m}} \tag{9}$$

which can be rewritten as follows:

$$\epsilon^2 \ddot{\boldsymbol{F}}_{\mathrm{t}} = -\boldsymbol{K}_0\left\{\boldsymbol{B}^{-1}\left[\boldsymbol{D}_{\mathrm{m}}\left(\epsilon^2 \boldsymbol{K}_0^{-1}\dot{\boldsymbol{F}}_{\mathrm{t}} + \dot{\boldsymbol{p}}\right) + \boldsymbol{F}_{\mathrm{t}} - \boldsymbol{F}_{\mathrm{m}}\right] + \ddot{\boldsymbol{p}}\right\}. \tag{10}$$

On the other hand, from (4) and (7), the time derivatives of $\boldsymbol{p}(\boldsymbol{q})$ can be expressed as follows:

$$\dot{\boldsymbol{p}} = -\dot{\boldsymbol{h}} = -\boldsymbol{P}(\boldsymbol{q})\dot{\boldsymbol{q}}; \quad \ddot{\boldsymbol{p}} = -\dot{\boldsymbol{P}}\dot{\boldsymbol{q}} - \boldsymbol{P}(\boldsymbol{q})\ddot{\boldsymbol{q}}. \tag{11}$$

Hence, substituting (11) into (14) yields[1]

$$\epsilon^2 \ddot{\boldsymbol{F}}_{\mathrm{t}} = \boldsymbol{K}_0\boldsymbol{B}^{-1}\left[\boldsymbol{F}_{\mathrm{m}} - \boldsymbol{F}_{\mathrm{t}} + \boldsymbol{D}_{\mathrm{m}}\left(\boldsymbol{P}\dot{\boldsymbol{q}} - \epsilon^2 \boldsymbol{K}_0^{-1}\dot{\boldsymbol{F}}_{\mathrm{t}}\right)\right] + \boldsymbol{K}_0\left(\dot{\boldsymbol{P}}\dot{\boldsymbol{q}} + \boldsymbol{P}\ddot{\boldsymbol{q}}\right). \tag{12}$$

Accordingly, from (2) and (9), we obtain the following dynamics for the whole system:

$$\ddot{\boldsymbol{q}} = -\boldsymbol{M}^{-1}\left[(\boldsymbol{C} + \boldsymbol{D})\dot{\boldsymbol{q}} + \boldsymbol{K}\boldsymbol{q} + \boldsymbol{g} + \boldsymbol{P}^\top \boldsymbol{F}_{\mathrm{t}}\right] \tag{13}$$

$$\begin{aligned}\epsilon^2 \ddot{\boldsymbol{F}}_{\mathrm{t}} = \boldsymbol{K}_0\Big\{&\left[\boldsymbol{B}^{-1}\boldsymbol{D}_{\mathrm{m}}\boldsymbol{P} + \dot{\boldsymbol{P}} - \boldsymbol{P}\boldsymbol{M}^{-1}(\boldsymbol{C} + \boldsymbol{D})\right]\dot{\boldsymbol{q}} \\ &- \boldsymbol{P}\boldsymbol{M}^{-1}(\boldsymbol{K}\boldsymbol{q} + \boldsymbol{g}) - \epsilon^2 \boldsymbol{B}^{-1}\boldsymbol{D}_{\mathrm{m}}\boldsymbol{K}_0^{-1}\dot{\boldsymbol{F}}_{\mathrm{t}} \\ &- \left(\boldsymbol{B}^{-1} + \boldsymbol{P}\boldsymbol{M}^{-1}\boldsymbol{P}^\top\right)\boldsymbol{F}_{\mathrm{t}} + \boldsymbol{B}^{-1}\boldsymbol{F}_{\mathrm{m}}\Big\}.\end{aligned} \tag{14}$$

To obtain the QSS value of the configuration variables and control input, we set $\epsilon = 0$ in (12)—or (14)—which, after some manipulations, yields[2]

$$\bar{\boldsymbol{F}}_{\mathrm{t}} = \boldsymbol{B}\left(\dot{\bar{\boldsymbol{P}}}\dot{\bar{\boldsymbol{q}}} + \bar{\boldsymbol{P}}\ddot{\bar{\boldsymbol{q}}}\right) + \boldsymbol{D}_{\mathrm{m}}\bar{\boldsymbol{P}}\dot{\bar{\boldsymbol{q}}} + \bar{\boldsymbol{F}}_{\mathrm{m}}. \tag{15}$$

Notice that we have set $\dot{\bar{\boldsymbol{F}}}_{\mathrm{t}} = \boldsymbol{0}$; this is required to guarantee that the fast system has an equilibrium. Finally, the QSS model is obtained by combining (13) and (15), which yields

$$\left(\bar{\boldsymbol{M}} + \bar{\boldsymbol{P}}^\top \boldsymbol{B}\bar{\boldsymbol{P}}\right)\ddot{\bar{\boldsymbol{q}}} + \left(\bar{\boldsymbol{C}} + \bar{\boldsymbol{P}}^\top \boldsymbol{B}\dot{\bar{\boldsymbol{P}}} + \boldsymbol{D} + \bar{\boldsymbol{P}}^\top \boldsymbol{D}_{\mathrm{m}}\bar{\boldsymbol{P}}\right)\dot{\bar{\boldsymbol{q}}} + \boldsymbol{K}\bar{\boldsymbol{q}} + \bar{\boldsymbol{g}} = -\bar{\boldsymbol{P}}^\top \bar{\boldsymbol{F}}_{\mathrm{m}}. \tag{16}$$

To obtain the expression for the BL model, it is necessary to define the new variable

$$\boldsymbol{y} := \boldsymbol{F}_{\mathrm{t}} - \bar{\boldsymbol{F}}_{\mathrm{t}} \tag{17}$$

which captures the variations around the quasisteady states. Note that the fast part of the system evolves much faster than (16) when $\epsilon$ tends to zero. Therefore, we can introduce a new time reference to analyze the dynamics (14). To this end, we define $v := (t - t_0)/\epsilon$, where $t_0 \in \mathbb{R}_+$ corresponds to the initial condition. Accordingly, from the chain rule, $\epsilon\dot{\boldsymbol{y}} = (d\boldsymbol{y})/(dv)$ and $\epsilon^2\ddot{\boldsymbol{y}} = (d^2\boldsymbol{y})/(dv^2)$. By substituting (15) and (17) into (12), setting $\bar{\boldsymbol{q}} = \boldsymbol{q}$, and considering the time derivatives of $\boldsymbol{F}_{\mathrm{t}}$ as zero,[3] we obtain the BL model, which is given by the following equation:

$$\frac{d^2\boldsymbol{y}}{dv^2} = -\epsilon\boldsymbol{B}^{-1}\boldsymbol{D}_{\mathrm{m}}\frac{d\boldsymbol{y}}{dv} - \boldsymbol{K}_0\left(\boldsymbol{B}^{-1} + \boldsymbol{P}\boldsymbol{M}^{-1}\boldsymbol{P}^\top\right)\boldsymbol{y} + \boldsymbol{K}_0\boldsymbol{B}^{-1}\boldsymbol{F}_{\mathrm{f}} \tag{18}$$

[1] We omit the arguments to ease the readability.

[2] The bar symbol, that is, $\bar{(\cdot)}$, is used to denote the QSS value of a variable or function. For instance, $\bar{\boldsymbol{P}} = \boldsymbol{P}(\bar{\boldsymbol{q}})$.

[3] Note that this is equivalent to the approach reported in [15].

where

$$\boldsymbol{F}_{\mathrm{f}} := \boldsymbol{F}_{\mathrm{m}} - \bar{\boldsymbol{F}}_{\mathrm{m}} \tag{19}$$

corresponds to the control signal used to modify the fast dynamics. Following the same rationale, $\bar{\boldsymbol{F}}_{\mathrm{m}}$ corresponds to the controller for the slow dynamics and $\boldsymbol{F}_{\mathrm{m}}$ is the sum of both control signals. An advantage of the proposed analysis is that we can independently design the controllers for the slow and fast subsystems. The following proposition provides such controllers and the corresponding closed-loop structures.

*Proposition 1:* Consider the QSS and BL models given by (16) and (18), respectively, the relation (19), and the control signals

$$\bar{\boldsymbol{F}}_{\mathrm{m}} = \left(\boldsymbol{I} + \boldsymbol{K}_{\mathrm{P}_2}\right) \boldsymbol{F}_{\mathrm{d}} - \boldsymbol{K}_{\mathrm{P}_2} \bar{\boldsymbol{F}}_{\mathrm{t}} \tag{20}$$

$$\boldsymbol{F}_{\mathrm{f}} = -\boldsymbol{K}_{\mathrm{P}_2} \boldsymbol{y} - \epsilon \boldsymbol{K}_{\mathrm{D}_2} \dot{\boldsymbol{y}} \tag{21}$$

where $\boldsymbol{K}_{\mathrm{P}_2}, \boldsymbol{K}_{\mathrm{D}_2} \in \mathbb{R}^{2\times 2}$ are positive definite (diagonal) gains and $\boldsymbol{F}_{\mathrm{d}} \in \mathbb{R}^2$ is a new control input to be designed. Define $\bar{\boldsymbol{K}}_{\mathrm{P}} := \boldsymbol{I} + \boldsymbol{K}_{\mathrm{P}_2}$. The closed-loop QSS and BL models take the form

$$\boldsymbol{M}_{\mathrm{q}} \ddot{\bar{\boldsymbol{q}}} = -\left(\boldsymbol{C}_{\mathrm{q}} + \boldsymbol{D}_{\mathrm{q}}\right) \dot{\bar{\boldsymbol{q}}} - \boldsymbol{K} \bar{\boldsymbol{q}} - \bar{\boldsymbol{g}} - \boldsymbol{P}^{\top} \boldsymbol{F}_{\mathrm{d}} \tag{22}$$

$$\frac{d^2 \boldsymbol{y}}{dv^2} = -\boldsymbol{K}_0 \boldsymbol{B}^{-1} \left( \boldsymbol{D}_{\mathrm{y}} \frac{d\boldsymbol{y}}{dv} + \boldsymbol{K}_{\mathrm{y}} \boldsymbol{y} \right) \tag{23}$$

where

$$\begin{aligned} &\boldsymbol{M}_{\mathrm{q}} := \bar{\boldsymbol{M}} + \bar{\boldsymbol{P}}^{\top} \bar{\boldsymbol{K}}_{\mathrm{P}}^{-1} \boldsymbol{B} \bar{\boldsymbol{P}}; \quad \boldsymbol{C}_{\mathrm{q}} := \bar{\boldsymbol{C}} + \bar{\boldsymbol{P}}^{\top} \bar{\boldsymbol{K}}_{\mathrm{P}}^{-1} \boldsymbol{B} \dot{\bar{\boldsymbol{P}}} \\ &\boldsymbol{D}_{\mathrm{q}} := \bar{\boldsymbol{D}} + \bar{\boldsymbol{P}}^{\top} \bar{\boldsymbol{K}}_{\mathrm{P}}^{-1} \boldsymbol{D}_{\mathrm{m}} \bar{\boldsymbol{P}}; \quad \boldsymbol{K}_{\mathrm{y}} := \bar{\boldsymbol{K}}_{\mathrm{P}} + \boldsymbol{B} \boldsymbol{P} \boldsymbol{M}^{-1} \boldsymbol{P}^{\top} \\ &\boldsymbol{D}_{\mathrm{y}} := \boldsymbol{K}_{\mathrm{D}_2} + \epsilon \boldsymbol{D}_{\mathrm{m}} \boldsymbol{K}_0^{-1}. \end{aligned} \tag{24}$$

Moreover, the total control law is given by the following equation:

$$\boldsymbol{F}_{\mathrm{m}} = \bar{\boldsymbol{K}}_{\mathrm{P}} \boldsymbol{F}_{\mathrm{d}} - \boldsymbol{K}_{\mathrm{P}_2} \boldsymbol{F}_{\mathrm{t}} - \epsilon \boldsymbol{K}_{\mathrm{D}_2} \dot{\boldsymbol{F}}_{\mathrm{t}}. \tag{25}$$

*Proof:* The closed-loop system (22) can be directly obtained by substituting (20) into (16). Nonetheless, a simpler way to get this expression consists of substituting (20) into (15) to obtain

$$\bar{\boldsymbol{F}}_{\mathrm{t}} = \bar{\boldsymbol{K}}_{\mathrm{P}}^{-1} \left[ \boldsymbol{B} \left( \dot{\bar{\boldsymbol{P}}} \dot{\bar{\boldsymbol{q}}} + \bar{\boldsymbol{P}} \ddot{\bar{\boldsymbol{q}}} \right) + \boldsymbol{D}_{\mathrm{m}} \bar{\boldsymbol{P}} \dot{\bar{\boldsymbol{q}}} \right] + \boldsymbol{F}_{\mathrm{d}}. \tag{26}$$

Then, substituting the above expression into (13) to get (22). The expression (23) is obtained by substituting (21) into (18) and using the definition of $\bar{\boldsymbol{K}}_{\mathrm{P}}$. The controller (25) is obtained by combining (20) and (21) and recalling that $\dot{\boldsymbol{y}} = \dot{\bar{\boldsymbol{F}}}_{\mathrm{t}}$. ■

This brief considers two approaches to designing $\boldsymbol{F}_{\mathrm{d}}$[4]

1) Pose regulation (PR) approach. The control input $\boldsymbol{F}_{\mathrm{d}}$ is given by the following equation:

$$\boldsymbol{F}_{\mathrm{d}} = -\boldsymbol{P}^{-\top} \left[ \boldsymbol{K} \boldsymbol{q}_{\star} + \boldsymbol{g}\left(\boldsymbol{q}_{\star}\right) - \boldsymbol{K}_{\mathrm{P}_1} \tilde{\boldsymbol{q}} - \boldsymbol{K}_{\mathrm{D}_1} \dot{\boldsymbol{q}} \right] \tag{27}$$

with $\tilde{\boldsymbol{q}} := \boldsymbol{q} - \boldsymbol{q}_{\star}$.

2) Proportional derivative plus (PD+) control: The signal $\boldsymbol{F}_{\mathrm{d}}$ is given by the following equation:

$$\begin{aligned} \boldsymbol{F}_{\mathrm{d}} = -\boldsymbol{P}^{-\top} \big[ &\boldsymbol{M}_{\mathrm{d}} \ddot{\boldsymbol{q}}_{\mathrm{d}} + \left(\boldsymbol{C}_{\mathrm{d}} + \boldsymbol{D}_{\mathrm{d}}\right) \dot{\boldsymbol{q}}_{\mathrm{d}} + \boldsymbol{K} \boldsymbol{q}_{\mathrm{d}} + \boldsymbol{g}\left(\boldsymbol{q}_{\mathrm{d}}\right) \\ &- \boldsymbol{K}_{\mathrm{P}_1} \tilde{\boldsymbol{q}}_{\mathrm{d}} - \boldsymbol{K}_{\mathrm{D}_1} \dot{\tilde{\boldsymbol{q}}}_{\mathrm{d}} \big] \end{aligned} \tag{28}$$

[4]For the implementation of $\boldsymbol{F}_{\mathrm{d}}$, we consider $\bar{\boldsymbol{q}} = \boldsymbol{q}$.

with $\tilde{\boldsymbol{q}}_{\mathrm{d}} := \boldsymbol{q} - \boldsymbol{q}_{\mathrm{d}}$ and

$$\begin{aligned} \boldsymbol{M}_{\mathrm{d}} &= \boldsymbol{M}\left(\boldsymbol{q}\right) + \boldsymbol{P}^{\top}\left(\boldsymbol{q}\right) \bar{\boldsymbol{K}}_{\mathrm{P}}^{-1} \boldsymbol{B} \boldsymbol{P}\left(\boldsymbol{q}\right) \\ \boldsymbol{C}_{\mathrm{d}} &= \boldsymbol{C}\left(\boldsymbol{q}, \dot{\boldsymbol{q}}\right) + \boldsymbol{P}^{\top}\left(\boldsymbol{q}\right) \bar{\boldsymbol{K}}_{\mathrm{P}}^{-1} \dot{\boldsymbol{P}}\left(\boldsymbol{q}, \dot{\boldsymbol{q}}\right) \\ \boldsymbol{D}_{\mathrm{d}} &= \boldsymbol{D} + \boldsymbol{P}^{\top}\left(\boldsymbol{q}\right) \bar{\boldsymbol{K}}_{\mathrm{P}}^{-1} \boldsymbol{D}_{\mathrm{m}} \boldsymbol{P}\left(\boldsymbol{q}\right). \end{aligned} \tag{29}$$

The complete control law is described by (25) together with (27) for the PR case and by (25) together with (28) for the PD+ approach.

An extensive exposition of standard PR and PD+ controllers applied to rigid robots is given in [19]. Furthermore, the stabilization properties of the PR approach for fully actuated and a class of underactuated soft robots are discussed in [21]. Similarly, the application of PD+ controllers to soft robots is reported in [1].

We remark that the inner-loop controller—given by the terms $-\boldsymbol{K}_{\mathrm{P}_2} \boldsymbol{F}_{\mathrm{t}}$ and $-\epsilon \boldsymbol{K}_{\mathrm{D}_2} \dot{\boldsymbol{F}}_{\mathrm{t}}$ in (25)—stiffens the tendons but not the robot. Indeed, the robot still behaves as a soft robot, preserving all the advantages of its compliant nature. Hence, the inner-loop controller counteracts the undesired effects that the tendons' compliance may cause between the actuators and the robot's body.

### A. Stability Analysis

Here, we provide a brief stability analysis for the closed-loop system considering $\boldsymbol{F}_{\mathrm{d}}$ as in (27). Similar arguments can be used for the PD+ case. However, those are omitted due to space limitations. For a thorough exposition of the stability analysis of slow-fast systems and SP methods, we refer the reader to [13], [14], and [20].

Note that (23) is a linear system (with respect to $\boldsymbol{y}$). Indeed, by defining $\boldsymbol{\eta} := [\boldsymbol{y}^{\top} \ \dot{\boldsymbol{y}}^{\top}]^{\top}$, we can write (23) as follows:

$$\dot{\boldsymbol{\eta}} = \boldsymbol{A}_{\eta} \boldsymbol{\eta}; \quad \boldsymbol{A}_{\eta} := \boldsymbol{K}_0 \boldsymbol{B}^{-1} \begin{bmatrix} \boldsymbol{0} & \boldsymbol{B} \boldsymbol{K}_0^{-1} \\ -\dfrac{1}{\epsilon^2} \boldsymbol{K}_{\mathrm{y}} & -\dfrac{1}{\epsilon} \boldsymbol{D}_{\mathrm{y}} \end{bmatrix}. \tag{30}$$

Because most matrices are diagonal and positive definite, a simple inspection shows that $\boldsymbol{K}_0 \boldsymbol{B}^{-1} \boldsymbol{K}_{\mathrm{y}}$ and $\boldsymbol{K}_0 \boldsymbol{B}^{-1} \boldsymbol{D}_{\mathrm{y}}$ are positive definite for any $\boldsymbol{q}$ and $t$. Hence, for any (constant) value of the former, $\boldsymbol{A}_{\eta}$ is Hurwitz, implying that the system (30) is exponentially stable. Furthermore, substituting the control law (27) into (22) yields

$$\boldsymbol{M}_{\mathrm{q}} \ddot{\bar{\boldsymbol{q}}} = -\left(\boldsymbol{C}_{\mathrm{q}} + \boldsymbol{D}_{\mathrm{q}} + \boldsymbol{K}_{\mathrm{D}_1}\right) \dot{\bar{\boldsymbol{q}}} - \left(\boldsymbol{K} + \boldsymbol{K}_{\mathrm{P}_1}\right) \tilde{\boldsymbol{q}} - \bar{\boldsymbol{g}} + \boldsymbol{g}\left(\boldsymbol{q}_{\star}\right). \tag{31}$$

Consider the Lyapunov function candidate

$$\begin{aligned} V\left(\bar{\boldsymbol{q}}, \dot{\bar{\boldsymbol{q}}}\right) = \frac{1}{2} \dot{\bar{\boldsymbol{q}}}^{\top} \boldsymbol{M}_{\mathrm{q}} \dot{\bar{\boldsymbol{q}}} + \frac{1}{2} \tilde{\boldsymbol{q}}^{\top} \left(\boldsymbol{K} + \boldsymbol{K}_{\mathrm{P}_1}\right) \tilde{\boldsymbol{q}} + \mathcal{E}\left(\bar{\boldsymbol{q}}\right) \\ - \mathcal{E}\left(\boldsymbol{q}_{\star}\right) - \tilde{\boldsymbol{q}}^{\top} \boldsymbol{g}\left(\boldsymbol{q}_{\star}\right) \end{aligned} \tag{32}$$

where $\mathcal{E}(\boldsymbol{q})$ is the gravitational potential energy. Thus, $(\partial \mathcal{E}(\boldsymbol{q}))/(\partial \boldsymbol{q}) = \boldsymbol{g}(\boldsymbol{q})$. Some simple computations show that

$$\dot{V} = -\dot{\tilde{\boldsymbol{q}}}^{\top} \left(\boldsymbol{D}_{\mathrm{q}} + \boldsymbol{K}_{\mathrm{D}_1}\right) \dot{\tilde{\boldsymbol{q}}} \leq 0. \tag{33}$$

Choose $\boldsymbol{K}_{\mathrm{P}_1}$ such that

$$\boldsymbol{K}_{\xi} := \boldsymbol{K} + \boldsymbol{K}_{\mathrm{P}_1} + \left. \frac{\partial \boldsymbol{g}\left(\boldsymbol{q}\right)}{\partial \boldsymbol{q}} \right|_{\boldsymbol{q}=\boldsymbol{q}_{\star}}$$

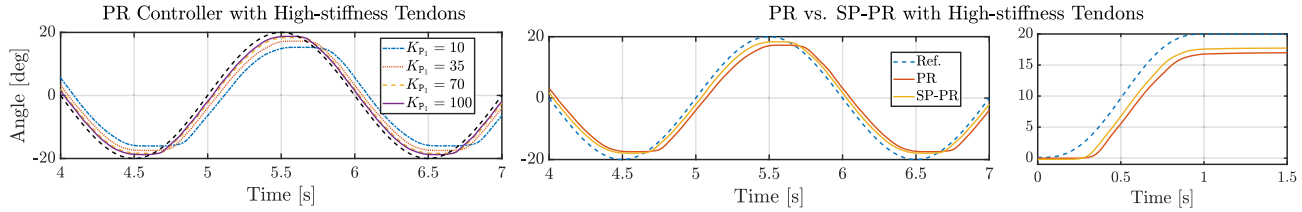


Fig. 3. Experimental results for PR and SP-PR controllers with high-stiffness tendons: the left-hand plot depicts the performance of the PR controller considering different gains $K_{P_1}$. The middle shows the comparison between the PR and SP-PR controllers while tracking a sinusoidal reference. Similarly, the right-hand plot provides a comparison of the same controllers tracking a step-like reference. The middle and right-hand plots correspond to the results obtained considering $K_{P_1} = 35$ and $K_{P_2} = 3$, respectively (for the SP-PR controller).

is positive definite. Hence, because $V(\boldsymbol{q}, \dot{\boldsymbol{q}})$ is positive definite with respect to $(\boldsymbol{q}_\star, \boldsymbol{0})$, (33) implies that (31) has a stable equilibrium at the desired equilibrium. Moreover, because $\boldsymbol{D}_q + \boldsymbol{K}_{D_1}$ is positive definite

$$\dot{V} = 0 \implies \dot{\tilde{\boldsymbol{q}}} = \boldsymbol{0} \implies \ddot{\tilde{\boldsymbol{q}}} = \boldsymbol{0} \implies \left(\boldsymbol{K} + \boldsymbol{K}_{P_1}\right)\tilde{\boldsymbol{q}} + \bar{\boldsymbol{g}} - \boldsymbol{g}\left(\boldsymbol{q}_\star\right) = \boldsymbol{0} \implies \bar{\boldsymbol{q}} = \boldsymbol{q}_\star.$$

Hence, it follows from LaSalle's invariance principle (see [20]) that the equilibrium is asymptotically stable. Finally, because $V(\boldsymbol{q}, \dot{\boldsymbol{q}})$ is radially unbounded, the stability properties are global.

Following the result of Thikonov's theorem (see [31, Th. 3.1] and [20, Th. 11.1 and 11.2]) or Fenichel's theorems (see [14, Th. 3]), the provided stability analyses are enough to guarantee that the differences $\boldsymbol{q} - \bar{\boldsymbol{q}}$ and $\boldsymbol{F}_t - \bar{\boldsymbol{F}}_t$ remain bounded for $\epsilon$ small. While this result is insufficient to ensure $\boldsymbol{q}$ tends to its desired value, it can be combined with a local analysis. To this end, we consider the following dynamics obtained from (13), (17), (15), and (20)

$$\boldsymbol{M}_q\ddot{\boldsymbol{q}} = -\left(\boldsymbol{C}_q + \boldsymbol{D}_q + \boldsymbol{K}_{D_1}\right)\dot{\boldsymbol{q}} - \left(\boldsymbol{K} + \boldsymbol{K}_{P_1}\right)\tilde{\boldsymbol{q}} - \boldsymbol{g} + \boldsymbol{g}\left(\boldsymbol{q}_\star\right) - \boldsymbol{P}^\top \boldsymbol{y}. \tag{34}$$

Define $\boldsymbol{\xi} = [\tilde{\boldsymbol{q}}^\top \quad \dot{\boldsymbol{q}}^\top]^\top$ and linearize (34) around the desired equilibrium. The resulting dynamics, together with (31), can be expressed as follows:

$$\begin{bmatrix}\dot{\boldsymbol{\xi}} \\ \dot{\boldsymbol{\eta}}\end{bmatrix} = \underbrace{\begin{bmatrix}\boldsymbol{A}_\xi & \boldsymbol{M}_q^{-1}\boldsymbol{P}^\top\left(\boldsymbol{q}_\star\right)\boldsymbol{A}_I \\ \boldsymbol{0} & \boldsymbol{A}_\eta\left(\boldsymbol{q}_\star\right)\end{bmatrix}}_{=:\boldsymbol{A}_T}\begin{bmatrix}\boldsymbol{\xi} \\ \boldsymbol{\eta}\end{bmatrix} \tag{35}$$

with

$$\boldsymbol{A}_I := \begin{bmatrix}\boldsymbol{0} & \boldsymbol{0} \\ -\boldsymbol{I} & \boldsymbol{0}\end{bmatrix}; \quad \boldsymbol{A}_\xi := \begin{bmatrix}\boldsymbol{0} & \boldsymbol{I} \\ -\boldsymbol{M}_q^{-1}\boldsymbol{K}_\xi & -\boldsymbol{M}_q^{-1}\left(\boldsymbol{D}_q + \boldsymbol{K}_{D_1}\right)\end{bmatrix}.$$

Note that $\boldsymbol{A}_T$ is a triangular matrix. Thus, its eigenvalues are determined by the eigenvalues of $\boldsymbol{A}_\xi$ and $\boldsymbol{A}_\eta$. Furthermore, the matrix $\boldsymbol{A}_\xi$ is Hurwitz—the analysis is omitted due to space limitations—implying that the system (35) is exponentially stable. Therefore, $\tilde{\boldsymbol{q}}$ tends to zero, indicating that $\boldsymbol{q}$ tends to $\boldsymbol{q}_\star$, as the time tends to infinity. This linearization-based analysis ensures the local exponential stability of the desired equilibrium for (34), which, combined with the boundedness of the trajectories, justifies the stability of the robot from a practical perspective.

TABLE I
SINUSOIDAL REFERENCE WITH HIGH-STIFFNESS TENDONS

| Metric [deg] | PR | PD+ | SP-PR | SP-PD+ |
|---|---|---|---|---|
| RMSE | 2.97 | 2.67 | 1.63 | 1.28 |
| SSE | 1.83 | 1.87 | 0.99 | 0.78 |
| Max. error | 4.45 | 4.04 | 2.28 | 2.19 |

## IV. EXPERIMENTAL RESULTS

We perform a series of experiments using the robot depicted in Fig. 1—which is based on the robots developed in [22]—to validate the effectiveness of the controllers derived from the SP approach, that is, (25)-(27) and (25)-(28), which are referred to as SP-PR and SP-PD+, respectively. To our knowledge, the results reported in this section are the first SP controllers for soft robots experimentally validated. Additionally, we compare the performance of the proposed controllers with traditional PR and PD+ strategies. To generate such controllers, we consider $\boldsymbol{F}_t = \boldsymbol{F}_d$, with $\boldsymbol{F}_d$ given by (27) for the PR approach and $\boldsymbol{F}_d$ described by (28) for the PD+ strategy. Additionally, we consider that the gain matrices have the following structure:

$$\boldsymbol{K}_{P_i} = K_{P_i}\boldsymbol{I}, \quad \boldsymbol{K}_{D_i} = K_{D_i}\boldsymbol{I}; \quad i \in \{1, 2\}.$$

We perform experiments using tendons with different stiffness coefficients: $k_{t_h} = 2.11 \times 10^4$ N/m and $k_{t_\ell} = 3.69 \times 10^3$ N/m. Then, we consider the root-mean-square error (RMSE), steady-state error (SSE), and maximum error as performance indices.

### A. High-Stiffness Tendons

We consider two reference signals: a sine wave and a step-like signal.[5] Both signals have an amplitude of 20°. As a first step, the PR controller is tested with several values for the gain $K_{P_1}$. The left-hand plot in Fig. 3 shows the performance of this controller following a sine trajectory, where we observe that the error decreases as the gain $K_{P_1}$ increases. These plots show that the SP approach outperforms the traditional controller. However, the improvement is relatively modest. To further assess the performance of the proposed controllers, Tables I and II show some performance metrics for the four controllers, that is, PR, PD+, SP-PR, and SP-PD+, with high-stiffness tendons. For comparison purposes, we fix $K_{P_1} = 35$ for all the controllers and $K_{P_2} = 1$ for the SP cases. The tables illustrate

[5]To have a smooth reference, we approximate the step signal with a seventh-order polynomial.

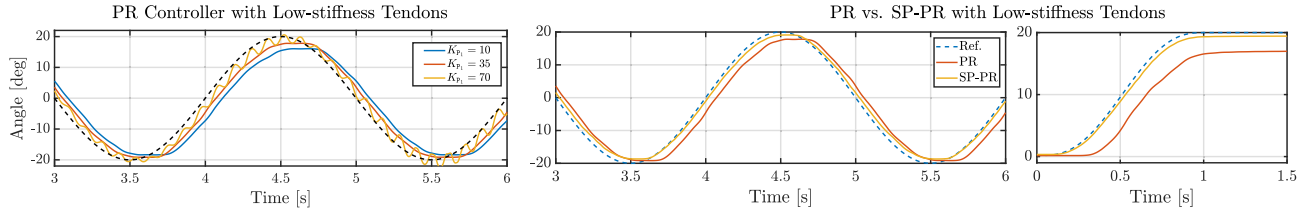


Fig. 4. Experimental results for PR and SP-PR controllers with low-stiffness tendons: the left-hand plot shows the performance of the PR controller considering different gains $K_{\mathrm{P}_1}$. The middle plot compares the PR and SP-PR controllers tracking a sinusoidal reference. Similarly, the right-hand plot provides a comparison of the same controllers tracking a step-like reference. The middle and right-hand plots correspond to the results obtained considering $K_{\mathrm{P}_1} = 35$ and $K_{\mathrm{P}_2} = 1$ (for the SP-PR controller).

TABLE II
STEP REFERENCE WITH HIGH-STIFFNESS TENDONS

| Metric [deg] | PR | PD+ | SP-PR | SP-PD+ |
|---|---|---|---|---|
| RMSE | 3.10 | 3.01 | 2.25 | 1.34 |
| SSE | 2.99 | 2.96 | 2.24 | 1.45 |
| Max. error | 4.26 | 4.12 | 2.99 | 1.65 |

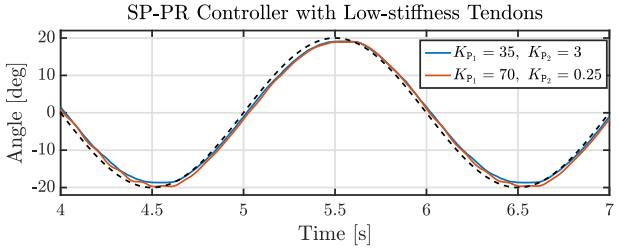


Fig. 5. Performance of the SP-PR controller with low tendon stiffness and different gains $K_{\mathrm{P}_1}$ and $K_{\mathrm{P}_2}$. The reference signal is the sine wave represented by the black dashed line.

that SP approaches exhibit much lower errors—more than 50% in some cases—than traditional feedback controllers.

Interestingly, increasing the gain $K_{\mathrm{P}_2}$ in the SP approaches results in undesired oscillatory behavior or even instability. This may be due to the high bandwidth of a high-stiffness tendon coupling. However, we stress that small SSE and RMSE can be achieved with much lower gains $K_{\mathrm{P}_1}$ than in the traditional feedback controllers.

*Remark 2:* The PR and PD+ controllers exhibit a decent performance if the control gains are increased—as shown in the left-hand plot in Fig. 3—because tendons with high stiffness guarantee that the approximation $\boldsymbol{F}_{\mathrm{t}} = \boldsymbol{F}_{\mathrm{m}}$ is valid. However, systems with more elastic tendons exhibit much poorer performance.

### B. Low-Stiffness Tendons

We conduct the same experiments as in Section IV-A but using low-stiffness tendons. In this case, increasing the gain $K_{\mathrm{P}_1}$ jeopardizes the closed-loop stability, as is illustrated by the left-hand plot in Fig. 4 for the PR controller. In fact, the system becomes unstable for $K_{\mathrm{P}_1} = 70$ and is unable to complete the trajectory. Concerning the SP controllers, the gain $K_{\mathrm{P}_2}$ plays an important role in improving the performance of the closed-loop system, where an appropriate selection of this gain permits tracking the reference with low and high values for $K_{\mathrm{P}_1}$ (see Fig. 5). The middle and right-hand plots of Fig. 4 compare the results obtained from implementing the PR and SP-PR controllers. In contrast to the high-stiffness case, the SP controller performs notoriously better. In particular, we point out that by tuning $K_{\mathrm{P}_2}$, the SP-PR controller exhibits a much lower SSE than the PR one when $K_{\mathrm{P}_1} = 35$. Similarly, an adequate selection of $K_{\mathrm{P}_2}$ drastically reduces the oscillations when $K_{\mathrm{P}_1}$ increases, which can be observed by comparing the case $K_{\mathrm{P}_1} = 70$ in the left-hand plot of Fig. 4 with Fig. 5. The supplementary video shows a visual comparison of the PD+ and SP-PD+ controllers, considering a high control gain ($K_{\mathrm{P}_1} = 70$), where it is evident that neglecting the dynamics of the actuators leads to instability. Tables III and IV show the performance of the four controllers with low-stiffness tendons. To compare the performance of the controllers, we fix $K_{\mathrm{P}_1} = 35$ for all the controllers and $K_{\mathrm{P}_2} = 3$ for the SP cases. The tables show that SP approaches exhibit much lower errors—at least 57% lower, but most more than 64% lower—than traditional feedback controllers. Fig. 6 summarizes the RMSEs obtained with the four controllers under analysis, considering two different references and high-stiffness and low-stiffness tendons. It is particularly notorious that SP controllers outperform traditional feedback approaches when the system is actuated using low-stiffness tendons. This is because as the tendons' stiffness decreases, the actuation dynamics are no longer negligible, and they play a more critical role in the motion of the continuum segment. Similarly, Fig. 7 compares the error evolution for the four controllers while tracking a sine wave with 20° of amplitude. This figure shows that SP controllers achieve more accurate reference tracking. An intuitive interpretation of these results is that SP approaches counteract the compliant nature of the low-stiffness tendons through an inner-loop controller.

TABLE III
SINUSOIDAL REFERENCE WITH LOW-STIFFNESS TENDONS

| Metric [deg] | PR | PD+ | SP-PR | SP-PD+ |
|---|---|---|---|---|
| RMSE | 3.16 | 2.98 | 1.12 | 0.90 |
| SSE | 1.87 | 1.93 | 0.25 | 0.33 |
| Max. error | 4.82 | 4.63 | 2.07 | 1.72 |

### C. Different Initial Conditions

To validate the robustness of the controllers with respect to the initial configuration of the robot, we generate random initial conditions that belong to a Gaussian distribution centered at 0° and consider a sinusoidal reference signal.

TABLE IV
STEP REFERENCE WITH LOW-STIFFNESS TENDONS

| Metric [deg] | PR | PD+ | SP-PR | SP-PD+ |
|---|---|---|---|---|
| RMSE | 2.38 | 2.23 | 0.67 | 0.60 |
| SSE | 1.83 | 1.82 | 0.58 | 0.59 |
| Max. error | 3.65 | 3.40 | 1.05 | 0.87 |

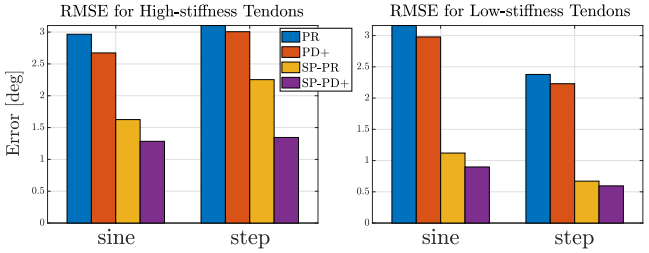


Fig. 6. RMSE for high-stiffness tendons (left) and low-stiffness tendons (right). The reference signals are a sine wave and a step, both with an amplitude of 20°. The gains for the high-stiffness case are $K_{\mathrm{P}_1} = 35$ (for all controllers) and $K_{\mathrm{P}_2} = 1$ (for SP controllers). Similarly, the gains for the low-stiffness case are $K_{\mathrm{P}_1} = 35$ (for all controllers) and $K_{\mathrm{P}_2} = 3$ (for SP controllers).


Fig. 7. Evolution of the error for the four tested controllers. The gains are $K_{\mathrm{P}_1} = 35$ (for all controllers) and $K_{\mathrm{P}_2} = 3$ (for SP controllers).

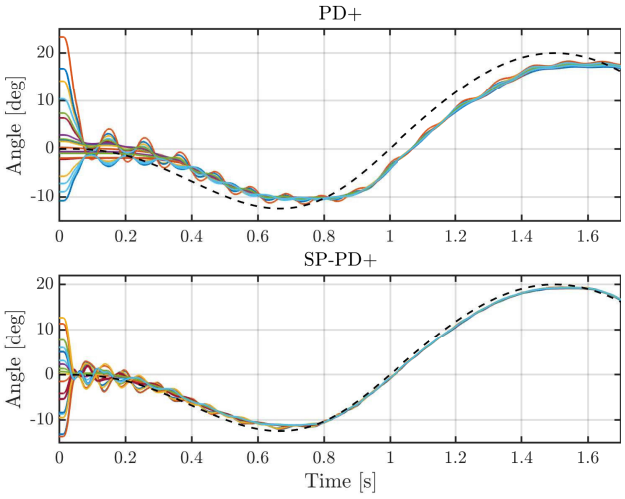


Fig. 8. Comparison between the PD+ and SP-PD+ controllers for different initial conditions. The desired trajectory is depicted with a black dashed line.

Moreover, these experiments are performed with low-stiffness tendons, using the same gain $K_{\mathrm{P}_1}$ in all the control strategies. A comparison between the PD+ and SP-PD+ controllers is presented in Fig. 8, where it is observed that the latter exhibits a smaller tracking error. Additionally, the PD+ controller still exhibits oscillations for certain initial conditions after one second, which does not occur in the SP-PD+ case.

TABLE V
PR VERSUS SP-PR UNDER DIFFERENT INITIAL CONDITIONS

| Metric [deg] | PR | SP-PR |
|---|---|---|
| RMSE | $3.37 \pm 0.14$ | $1.18 \pm 0.08$ |
| SSE | $2.09 \pm 0.19$ | $0.33 \pm 0.09$ |
| Max. error | $8.24 \pm 3.71$ | $7.49 \pm 3.91$ |

TABLE VI
PD+ VERSUS SP-PD+ UNDER DIFFERENT INITIAL CONDITIONS

| Metric [deg] | PD+ | SP-PD+ |
|---|---|---|
| RMSE | $3.01 \pm 0.08$ | $0.99 \pm 0.09$ |
| SSE | $1.94 \pm 0.07$ | $0.35 \pm 0.04$ |
| Max. error | $8.17 \pm 5.02$ | $6.41 \pm 4.02$ |

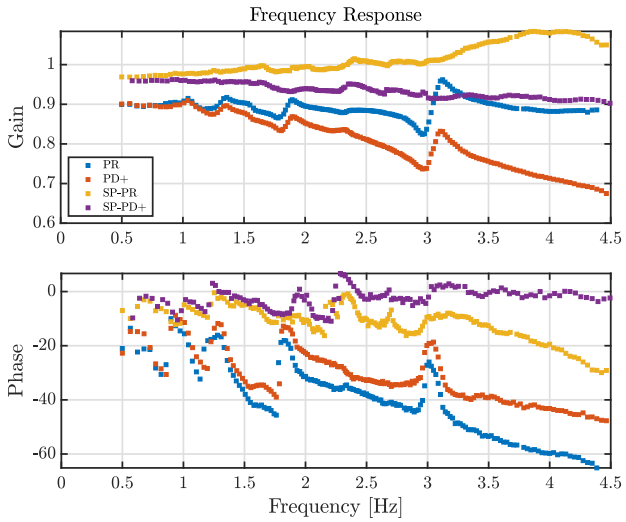


Fig. 9. Frequency responses of the four tested controllers. The upper figure corresponds to the gain, while the lower figure shows the phase.

Tables V and VI provide a performance comparison between the PR and SP-PR controllers and the PD+ and SP-PD+ controllers, respectively. In both cases, the SP controllers perform better than traditional feedback versions. Consequently, we conclude that SP controllers converge faster to the desired trajectory under similar initial conditions and are more accurate than conventional feedback controllers.

### D. Frequency Response

To study the frequency response of the closed-loop system, we consider a chirp signal as the reference, performing experiments for each control approach. The reference frequency varies slowly from 0.5 to 4.5 Hz. The gain and phase for each controller are depicted in Fig. 9, while the RMSEs are shown in Fig. 10. From these plots, we make the following observations.

1) The PR and PD+ strategies show poorer performances as the frequency increases. Both control strategies exhibit a decrement in gain at a frequency close to 3 Hz followed by a peak. While its gain does not tend to decrease at high frequencies, the PR strategy exhibits the most significant phase lag (more than 60°) and the highest RMSE (around 15°). On the other hand, the gain

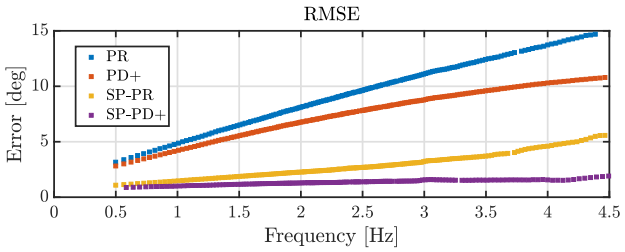


Fig. 10. RMSEs in the frequency spectrum for the different controllers.

of the PD+ controller decreases drastically as the frequency increases. This control strategy exhibits the second worst values for phase lag and RMSE.

2) The SP-PR controller shows considerable improvement with respect to the PR strategy. In particular, it shows a smaller phase lag and RMSE. However, this controller's gain increases at high frequencies. Moreover, the RMSE and phase lag increase as the frequency increases, making it unsuitable for trajectory tracking at high frequencies.
3) The SP-PD+ controller exhibits better performance than the other strategies. In particular, it shows a minor gain loss, lower phase lag at high frequencies, and a smaller RMSE compared with the other three control approaches. This controller is the only one—among the four tested strategies—suitable for trajectory tracking at high frequencies.

## V. Concluding Remarks

This brief proposed two SP control strategies for planar tendon-driven soft robots. These strategies are suitable for considering the dynamics of the actuation system. A series of experiments were performed to: 1) validate the effectiveness of the proposed controllers and 2) compare their performance with traditional feedback controllers that neglect the dynamics of the actuation system. The experimental results show that the proposed SP strategies exhibit better performance than traditional feedback approaches, especially as the stiffness of the tendons decreases.

## References

[1] C. Della Santina, C. Duriez, and D. Rus, "Model-based control of soft robots: A survey of the state of the art and open challenges," *IEEE Control Syst.*, vol. 43, no. 3, pp. 30–65, Jun. 2023.

[2] B. Caasenbrood, A. Pogromsky, and H. Nijmeijer, "Energy-shaping controllers for soft robot manipulators through port-Hamiltonian cosserat models," *Social Netw. Comput. Sci.*, vol. 3, no. 6, p. 494, Sep. 2022.

[3] P. Pustina, P. Borja, C. Della Santina, and A. De Luca, "P-satI-D shape regulation of soft robots," *IEEE Robot. Autom. Lett.*, vol. 8, no. 1, pp. 1–8, Jan. 2023.

[4] M. Stolzle and C. Della Santina, "Piston-driven pneumatically-actuated soft robots: Modeling and backstepping control," *IEEE Control Syst. Lett.*, vol. 6, pp. 1837–1842, 2022.

[5] M. Russo et al., "Continuum robots: An overview," *Adv. Intell. Syst.*, vol. 5, no. 5, Mar. 2023, Art. no. 2200367.

[6] P. Rao, Q. Peyron, S. Lilge, and J. Burgner-Kahrs, "How to model tendon-driven continuum robots and benchmark modelling performance," *Frontiers Robot. AI*, vol. 7, Feb. 2021, Art. no. 630245.

[7] F. Janabi-Sharifi, A. Jalali, and I. D. Walker, "Cosserat rod-based dynamic modeling of tendon-driven continuum robots: A tutorial," *IEEE Access*, vol. 9, pp. 68703–68719, 2021.

[8] A. Shu, B. Deutschmann, A. Dietrich, C. Ott, and A. Albu-Schäffer, "Robust $H_\infty$ control of a tendon–driven elastic continuum mechanism via a systematic description of nonlinearities," *IFAC-PapersOnLine*, vol. 51, no. 22, pp. 386–392, 2018.

[9] E. Amanov, T.-D. Nguyen, and J. Burgner-Kahrs, "Tendon-driven continuum robots with extensible sections—A model-based evaluation of path-following motions," *Int. J. Robot. Res.*, vol. 40, no. 1, pp. 7–23, 2021.

[10] H. Li, L. Xun, G. Zheng, and F. Renda, "Discrete cosserat static model-based control of soft manipulator," *IEEE Robot. Autom. Lett.*, vol. 8, no. 3, pp. 1739–1746, Mar. 2023.

[11] C. A. Monje, B. Deutschmann, J. Muñoz, C. Ott, and C. Balaguer, "Fractional order control of continuum soft robots: Combining decoupled/reduced-dynamics models and robust fractional order controllers for complex soft robot motions," *IEEE Control Syst.*, vol. 43, no. 3, pp. 66–99, Jun. 2023.

[12] R. J. Webster and B. A. Jones, "Design and kinematic modeling of constant curvature continuum robots: A review," *Int. J. Robot. Res.*, vol. 29, no. 13, pp. 1661–1683, Nov. 2010.

[13] P. Kokotović, H. K. Khalil, and J. O'Reilly, *Singular Perturbation Methods in Control: Analysis and Design*. Philadelphia, PA, USA: SIAM, 1999.

[14] H. Jardón-Kojakhmetov, J. M. A. Scherpen, and D. D. Puerto-Flores, "Stabilization of a class of slow–fast control systems at non-hyperbolic points," *Automatica*, vol. 99, pp. 13–21, Jan. 2019.

[15] C. Ott, A. Albu-Schaffer, and G. Hirzinger, "Comparison of adaptive and nonadaptive tracking control laws for a flexible joint manipulator," in *Proc. IEEE/RSJ Int. Conf. Intell. Robots Syst.*, vol. 2, Sep. 2002, pp. 2018–2024.

[16] T. Shi, Y. Pan, and C. Wen, "Modern compliant robot control: Exploring benefits from singular perturbation synthesis," *IEEE Trans. Ind. Electron.*, vol. 72, no. 3, pp. 2758–2768, Mar. 2025.

[17] H. Kobayashi and R. Ozawa, "Adaptive neural network control of tendon-driven mechanisms with elastic tendons," *Automatica*, vol. 39, no. 9, pp. 1509–1519, Sep. 2003.

[18] M. A. Khosravi and H. D. Taghirad, "Dynamic modeling and control of parallel robots with elastic cables: Singular perturbation approach," *IEEE Trans. Robot.*, vol. 30, no. 3, pp. 694–704, Jun. 2014.

[19] R. Kelly, V. Santibáñez, and A. Loría, *Control of Robot Manipulators in Joint Space*. Berlin, Germany: Springer, 2005.

[20] H. K. Khalil, *Nonlinear Systems*, 3rd ed., Upper Saddle River, NJ, USA: Prentice-Hall, 2002.

[21] P. Borja, A. Dabiri, and C. Della Santina, "Energy-based shape regulation of soft robots with unactuated dynamics dominated by elasticity," in *Proc. IEEE 5th Int. Conf. Soft Robot. (RoboSoft)*, Apr. 2022, pp. 396–402.

[22] J. Reinecke, B. Deutschmann, and D. Fehrenbach, "A structurally flexible humanoid spine based on a tendon-driven elastic continuum," in *Proc. IEEE Int. Conf. Robot. Autom. (ICRA)*, May 2016, pp. 4714–4721.